Title

Measurement of Diurnal Variation in Rod Outer Segment Length In Vivo in Mice With the OCT Optoretinogram

Journal

Investigative Ophthalmology & Visual Science, 61(3)

ISSN

0146-0404

Authors

Zhang, Pengfei
Shibata, Bradley
Peinado, Gabriel
et al.

Publication Date

2020-03-16

DOI

10.1167/iovs.61.3.9

Peer reviewed

Measurement of Diurnal Variation in Rod Outer Segment Length In Vivo in Mice With the OCT Optoretinogram

Pengfei Zhang,[1] Bradley Shibata,[2] Gabriel Peinado,[2] Robert J. Zawadzki,[1,3] Paul FitzGerald,[2] and Edward N. Pugh Jr[1]

[1]UC Davis Eye-Pod, Department of Cell Biology and Human Anatomy, University of California Davis, Davis, California, United States
[2]Department of Cell Biology and Human Anatomy, School of Medicine, University of California Davis, Davis, California, United States
[3]Vision Science and Advanced Retinal Imaging Laboratory (VSRI), Department of Ophthalmology & Vision Science, University of California Davis, Sacramento, California, United States

Correspondence: Edward N. Pugh Jr, UC Davis, 3301 Tupper Hall, Davis, CA 95616, USA; enpugh@ucdavis.edu.

Received: June 19, 2019
Accepted: November 25, 2019
Published: March 16, 2020

Citation: Zhang P, Shibata B, Peinado G, Zawadzki RJ, FitzGerald P, Pugh EN Jr. Measurement of diurnal variation in rod outer segment length in vivo in mice with the OCT optoretinogram. *Invest Ophthalmol Vis Sci.* 2020;61(3):9. https://doi.org/10.1167/iovs.61.3.9

Purpose. To investigate diurnal variation in the length of mouse rod outer segments in vivo.

Methods. The lengths of rod inner and outer segments (RIS, ROS) of dark-adapted albino mice maintained on a 12-hour dark:12-hour light cycle with light onset 7 AM were measured at prescribed times (6:30 AM, 11 AM, 3:30 PM) during the diurnal cycle with optical coherence tomography (OCT), taking advantage of increased visibility, after a brief bleaching exposure, of the bands corresponding to RIS/ROS boundaries and ROS tips (ROST).

Results. Deconvolution of OCT depth profiles resolved two backscatter bands located 7.4 ± 0.1 and 10.8 ± 0.2 µm (mean ± SEM) proximal to Bruch's membrane (BrM). These bands were identified with histology as arising from the apical surface of RPE and ROST, respectively. The average length of dark-adapted ROS at 6:30 AM was 17.7 ± 0.8 µm. By 11 AM, the average ROS length had decreased by 10% to 15.9 ± 0.7 µm. After 11 AM, the ROS length increased steadily at an average rate of 0.12 µm/h, returning to baseline length by 23.5 hours in the cycle.

Conclusions. The diurnal variation in ROS length measured in these experiments is consistent with prior histological investigations showing that rodent rod discs are phagocytosed by the RPE maximally over several hours around the time of normal light onset. The rate of recovery of ROS to baseline length before normal light onset is consistent with the hypothesis that disc membrane synthesis is fairly constant over the diurnal cycle.

Keywords: rods outer segments, photoreceptor, opto-physiology, in vivo imaging, optical coherence tomography

Rods and cones are the principal types of photoreceptors in the vertebrate retina. As in the human eye, photoreceptors in the mouse outnumber all other retinal cell types by 20-fold or more. Moreover, as in the human retinal periphery, rods are the dominant type of photoreceptors in the mouse, with a well-established ratio to cones of 30:1,[1] very similar to that of the human periphery at eccentricities exceeding 20°.[2,3] The numerosity of rods makes rhodopsin the most abundant retinal protein, and further makes the retina especially vulnerable to rod-specific genetic diseases, such as missense or null mutations in rhodopsin that give rise to retinitis pigmentosa.[4–6] Because photoreceptors transduce light into the electrical signals that initiate vision,[7] mutations and oxidative or other damage to photoreceptor proteins and lipids lead to vision loss and often blindness.

Since the seminal work of Richard Young,[8–10] it has been understood that the outer segments of rods and cone photoreceptors are continually renewed, a process that replaces damaged proteins and lipids. In mammals, disc membranes comprising about one-tenth of the outer segment are newly synthesized every day at the base of the outer segment. Homeostasis of outer segment length is achieved by RPE cell phagocytosis on average of the same number of discs at the outer segment tips. Investigations of outer segment renewal have largely been undertaken with histology, either by measuring the translation along the outer segment of radiolabeled disc membranes, or by quantification of disc membrane phagosomes in the RPE. Recent investigations with optical coherence tomography (OCT) of individual human cones have found results interpretable as cone outer segment length shortening associated with disc phagocytosis, and as lengthening expected from diurnal renewal,[11–13] though to our knowledge there have been no similar reports about rods of any species. Despite a substantial body of research,[14–25] the cellular and molecular mechanisms governing outer segment renewal and disc shedding remain an ongoing topic of

investigation.[26–32] Given the importance of the mouse as a model organism for the investigation of the mechanisms of ocular function and disease,[33–37] it would be valuable to be able to noninvasively measure rod outer segment (ROS) renewal in vivo in the mouse.

OCT can generate micrometer-resolution depth profiles (A-scans) of the living mouse retina,[38–41] and has become increasingly valuable for studying both structure and function in the photoreceptor layer. Recent investigations in mice and humans with OCT have shown that ROS and/or cone OS elongate in response to stimuli that bleach substantial fractions of their rhodopsin.[42–45] In mouse rods, this elongation has been established to be driven by phototransduction because it requires expression of the rod G-protein transducin.[42] Given the capability of OCT to measure submicrometer ROS length changes after suitable averaging and analysis,[42] we undertook an investigation to determine whether OCT could also be used to measure diurnal ROS length changes arising from disc shedding and renewal.

In this paper, we have adopted the term "optoretinogram" (ORG) for the OCT experimental paradigm used. The term ORG was coined by Don MacLeod[46] upon considering a paper on bleaching-induced changes in near-infrared (NIR) light transmission in toad retina.[47] The term has been recently adopted by other investigators[48] (Pandiyan et al.; IOVS 2019;60; ARVO E-Abstract 1426) for the paradigm of using NIR OCT to measure bleaching-induced backscattering and/or elongation changes in the eye in vivo noninvasively.[42–45,49] We think the term deserves general adoption in vision and ophthalmology, as ORG draws an instructive parallel to the ERG, which has long been used to assess retinal function in vivo. Specifically, the ORG, like the ERG, comprises multiple components arising from distinct cells and mechanisms. Moreover, both ERG and ORG require an explanation in terms of the underlying cellular and molecular mechanisms to achieve their full scientific and clinical utility. We suggest, however, that the term optoretinogram should serve primarily as a description of the experimental paradigm and the "raw" traces, and that the term optophysiological response continue to be used to describe bleaching-induced changes attributabled to specific cells and cellular and molecular mechanisms. In other words, the ORG refers to an experimental method used to measure retinal responses to visible light stimuli.

Methods

Animal Husbandry, Anesthesia, and Experimental Protocols

All mouse husbandry and handling were in accord with protocols approved by the University of California Animal Care and Use Committee, which strictly adheres to all National Institutes of Health guidelines and satisfies the ARVO guidelines for animal use. Because the lack of melanin in albino mice allows clear visualization of backscatter from ROS tips (ROST) and from BrM, only albino mice, including Balb/c and B6-albinos (B6(Cg)-*Tyr*$^{c-2J}$/J) mice, were used for this study. Mice were obtained from Jackson Labs at age 2 months and maintained on a 12D:12L (~100 lux) light cycle, and were between 2 and 8 months of age at the time of experimentation. A contact lens and gel (GelTeal Tears, Alcon) were used to maintain corneal transparency.[50–52] Mice were dark-adapted overnight, and between sessions when there were multiple experiments per day (described in the next paragraph). All experiments were performed in a completely darkened room. During the experiments mice were anesthetized with 2% isoflurane delivered in O_2, and maintained on a heated, adjustable platform adjacent to the imaging apparatus, as described previously.[51]

Balb/c mice were used in the initial phase of the investigation that uncovered the novel scattering band attributed to the ROST. The experiments performed to measure diurnal variation in ROS length were performed on B6-albino mice, in part to achieve maximum comparability with previously published studies of disc shedding in normally pigmented B6 mice, which are congenic with B6 albinos save for the null mutation in the tyrosinase gene that eliminates melanin. Based on published measurements of disc shedding[22] and the light onset time (7:00 AM) in our vivarium, we selected three times in the diurnal cycle for ROS length measurements: 6:30 AM, 11 AM, and 3:30 PM, anticipating that 6:30 AM would precede, whereas 11 AM and 3:30 PM would follow, the dominant phase of shedding.

We adopted a "within-subjects" design for the study to minimize between-subject variation that could affect the reliability of the measurements of ROS length changes. Accordingly, 6:30 AM was fixed as a standard time of day at which baseline OCT measurements were made in mice dark-adapted overnight, followed by a single 10% bleaching exposure and OCT to measure the saturating optophysiological responses of the rods.[42] The 6:30 AM baseline data of each mouse in a given day's experiment were then used to assess diurnal changes in rod outer segment length in that mouse and retinal location. This design required mice to be subjected to up to three exposures to isoflurane anesthetic during a day. The consequences of these multiple exposures to anesthetic were assumed to be negligible, as gaseous isoflurane is very rapidly eliminated after the animal is removed from the source,[53] as manifest by return to normal mobility and other cage behaviors within ~5 minutes of removal from the anesthetic delivery system. Mice were dark-adapted for the entire time between imaging sessions. Based on published measurements of rhodopsin regeneration in mice in vivo,[54] the minimal 2-hour interval between sessions ensured complete regeneration from the 10% bleaching exposure. In addition, as described in the Results, reflected light from the NIR (860 nm) OCT source captured by the SLO arm of the multimodal imaging apparatus (described in the following section) was used to position the mouse so that the same fundus region of the same eye was imaged and bleached in each session while negligibly activating phototransduction. Specifically, the total 860-nm energy density in an experimental session did not exceed 2.5 J cm^{-2}, and because the absorption coefficient of mouse rhodopsin is reduced by 9 $\log_{10}$ units at 860 nm relative to that at its λ_{max} (498 nm), a 2.5 J cm^{-2} exposure would on average produce ~1 bleached rhodopsin per rod).[51] Experiments were only performed on one eye on any given day.

For the OCT experiments performed to resolve the scattering band attributed to the ROST (data shown in Fig. 2 and Fig. 3), 6 animals (11 eyes) were studied. For the experiments used to measure diurnal changes in ROS length (Fig. 5 and Fig. 6), 6 animals (12 eyes) were studied, and 3 sessions were performed on each animal. For histology (Fig. 3), 3 animals (6 eyes) were sacrificed and prepared.

Mouse Multimodal In Vivo Imaging System

A custom multimodal SLO/OCT system was used for in vivo imaging of the mouse retina.[55] The SLO subsystem is equipped with a 488-nm laser (Coherent, 488-30FP) with an external trigger that enables precise control of light delivery during scanning.[51] The SLO was used to deliver precisely calibrated 488-nm bleaching exposures.[51] The SLO system can also capture a small portion of the back-reflected NIR OCT light (i.e., that reflected by the dichroic mirror that combines the incoming SLO and OCT beams). Operating in this matter the SLO was used for alignment of the mouse; otherwise the SLO was only used for delivery of the 488-nm light for bleaching. The SLO laser power was set to 9.4 µW at the mouse pupil. A single SLO scan at this power bleaches ~10% of the rhodopsin.[51] The NIR Fourier domain-OCT system has a superluminescent diode light source (Superlum, T-860-HP) with an 82-nm bandwidth (effective full-width at half maximum [FWHM] after Hann windowing) centered at 860 nm, and delivers 600 µW at the mouse pupil. The total 860-nm light exposure during an imaging session produced negligible bleaching or activation of rhodopsin (see the previous section).

Standard Protocol for In Vivo Imaging of the Rod ORG

The timing protocol and the spatial arrangement of the OCT scanning and SLO bleaching are illustrated in Figures 1A and B, respectively. The blue-green rectangular area in Figure 1B represents the bleach field, which subtended 50° of visual angle laterally and 25° vertically, and mapped to 512 digital samples (pixels) laterally and 128 pixels vertically. The conversion from degrees to linear distance on the retina depends primarily on the optics of the mouse eye, but also to some extent on the contact lens and the thickness of the gel layer between the contact lens and the cornea. Based on our prior analysis of these factors,[52] we estimate the conversion coefficient for these experiments to be ~36 µm/degree. The mouse optic nerve head (white arrow in the lower left of Fig. 1B) was aligned away from the center of the image field to optimize uniformity of retinal thickness in the B-scan field. An individual experiment consisted of a series of scanning cycles with 4 B-scans collected in each cycle, with the following exceptions. Initially, 20 cycles comprising 80 B-scans were collected from the dark-adapted retina for baseline measurements, and then on the 21st scan cycle, the 488-nm laser was triggered to deliver the bleaching exposure. The scanning cycle continued for ~5 minutes to record the rod optophysiological response.[42] Each cycle took ~0.92 seconds, including ~0.22 seconds for data transfer and scanner resetting time (Fig. 1A). The scanning protocol was designed to optimize the use of system memory and to ensure that the data acquired with OCT come entirely from the bleached region.

Image Processing for the Standard ORG Protocol

OCT spectra were Fourier transformed after 4× zero-padding[56] and the resultant A-scan profiles remapped onto a linear, 16-bit unsigned scale. To obviate the effect on length measurement of low quality OCT A-scans in two sides of the B-scan, an ~35° center portion of the 50° wide B-scan field was used for analysis (green dashed rectangle in Fig. 1B). The semiautomated postprocessing can be divided into three steps:

1. Initial alignment: All the OCT B-scans from an experiment were first stacked in a time series (Fig. 1C), and then subdivided laterally into substacks (k = 1, 2, …, n, Fig. 1C) to maximize similarity among the A-scans initially processed together. Each substack obtained at a given time comprised 80 A-scans; these 80 A-scans were first aligned by cross-correlation and then averaged. The averaged A-scans obtained from each substack were then aligned over time. Next, at each depth (axial pixel location) the median value of each set of five successive average A-scans was taken; this effectively suppresses occasional motion artifacts arising from mouse breathing. These steps generate a "kymograph" (Fig. 1D), representing the changes in each averaged substack over time as an depth versus time image [i.e., $I(z, t)$ vs. t, where I is backscatter intensity, z depth, and t time].
2. Fine alignment: In albino mice, scattering by BrM gives rise to an exceptionally sharp hyperreflective band (Fig. 1E, whose FWHM is very close to the predicted Gaussian approximation of the OCT point-spread function (PSF), with FWHM of 3.6 µm in our system. The kymographs from each substack were aligned to BrM, and then averaged to obtain the grand average axial scattering profile for each time point (Fig. 1E, "average"). (We note that the appearance of the BrM-to-ROST complex is different in this report from that in another recent report from our laboratory[57] because different OCT systems were used; in the latter investigation[57] a swept-source system with longer center wavelength (1060 nm vs. 860 nm for this study) and poorer axial resolution (axial PSF FWHM of 5.6 µm vs. 3.6 µm for this study), but greater axial range was used.
3. Further analysis: The Fourier Domain OCT A-scan profile corresponds to the axial tissue reflectivity or backscatter distribution of the posterior eye convolved with the OCT axial PSF, combined with system noise including the electrical noise of the photodetector, shot noise, and relative intensity noise from the reference arm light.[58] The axial PSF in OCT is determined by the source bandwidth, and is usually approximated by a Gaussian,[40] whose standard formulation predicts the PSF of our OCT to be a Gaussian with FWHM of 3.6 µm. In an effort to extract additional information from the hyperreflective bands, we used deconvolution, a method widely used in image processing to sharpen images and uncover detail. Specifically, the averaged line profile data were deconvolved with the MATLAB "deconvlucy" function using the axial PSF as the mathematical kernel (argument in the function call), and the hyperreflective bands from each time point fitted with Gaussian functions providing three parameters (position, amplitude, and FWHM) that were used for further analysis (Fig. 2C).

Imaging Protocol for Measuring Diurnal Variation in ROS Length with Volumetric Data Acquisition

The design of experiments aimed at measuring diurnal changes in ROS length needed to satisfy a number of criteria,

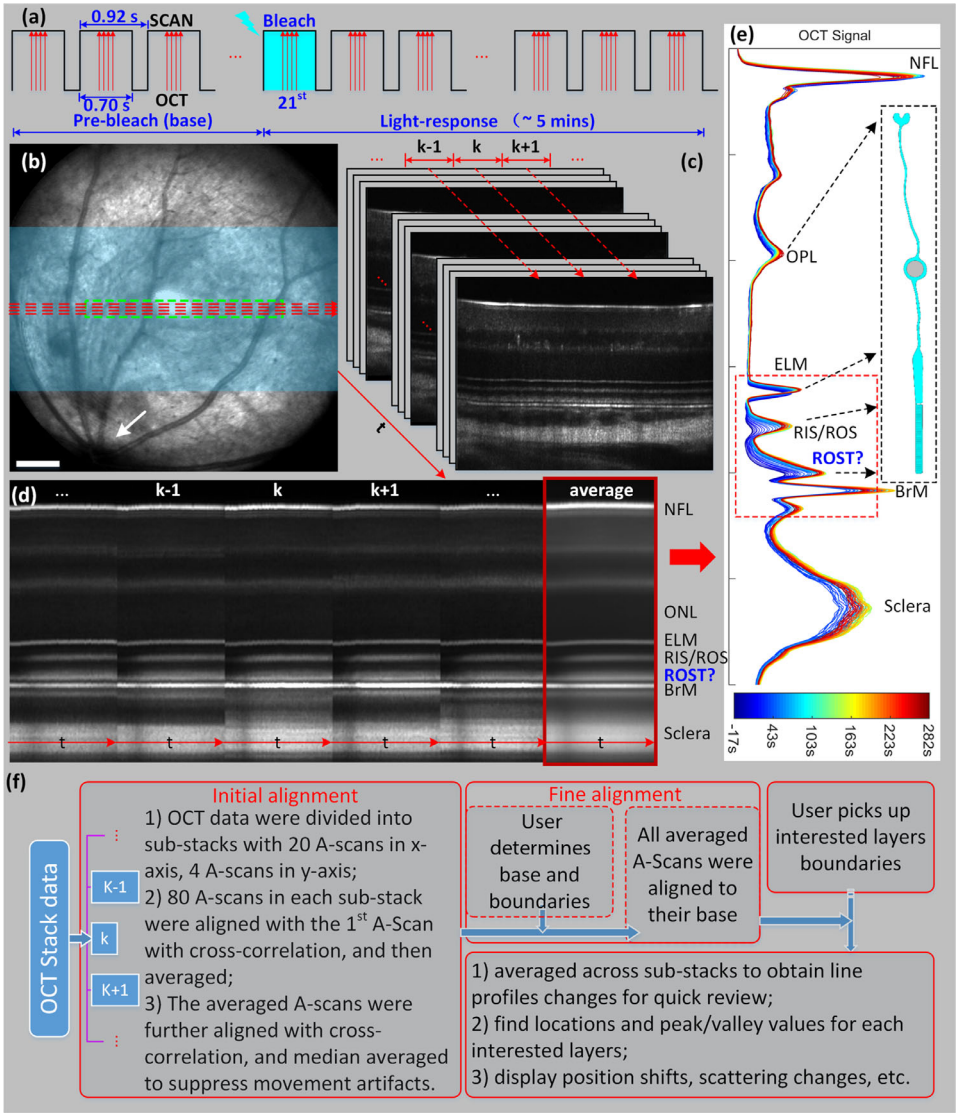

Figure 1. Stimulation, imaging, and OCT data processing protocols. (**a**) Timing of the scanning protocol: once every 0.92 seconds 4 OCT B-scans were taken (red arrows); during the 21st scan cycle a 488-nm stimulus that bleached ~10% of the rhodopsin was delivered by the SLO; the scanning cycle continued after the bleaching exposure for ~5 minutes. (**b**) En face SLO image of the retina, indicating the bleach field (blue-green overlay) and the location of the B-scans (red dashed arrows); the green rectangle shows the subregion used for analysis. (**c**) Illustration of the spatial and temporal processing of the OCT B-scan data. The symbol *t* represents time, while k = 1, …, n (typically n = 15–20) identify 80 µm wide subregions of the B-scan data stacks used in the analysis; (**d**) postprocessed "kymograph" presentations of average A-scan backscatter intensity profiles from each substack, showing how these profiles evolve in time; the kymograph averaged over the substacks is presented at right (average) with layer identifications. (**e**) Grand average A-scan profiles for different time points superimposed, and color-coded for time as indicated by the color bar); the red dashed rectangle identifies the portion of the profiles used for analysis of rod length and scattering, while the cyan inset provides a cartoon model of single rod drawn approximately to scale, with the dashed black arrows identifying relating the hyperreflective bands to locations on the cartoon, and question marks indicating bands whose source is investigated. (**f**) Summary of the image processing flow chart for the standard ORG protocol. NFL, nerve fiber layer; OPL, outer plexiform layer. Length scale bar in (**b**): 250 µm.

including in particular the need to image the same region of the retina of individual mice at multiple sessions during the diurnal cycle. To ensure that the same retinal region was measured, the imaging protocol described in the previous section was slightly modified: instead of acquiring just four B-scans in the center of the bleached regions on each cycle, a full OCT volume of the bleaching field was acquired every fourth scanning cycle. Postprocessing of the volumetric data employed the same procedures, with the addition of a minor change at the end of the fine alignment: the aligned A-scan data from the entire volume were averaged to obtain the grand average line profile at the time points when volumes were acquired. Because OCT scanning in the vertical (dorso-ventral) dimension extended over a relatively large distance, some variation in A-scan line profiles over this dimension was anticipated, as had been found in the comparable wide horizontal direction. Averaging over such variation would alter the precision of measurement of weak intensity peaks, such as those arising from the RIS/ROS and ROST scattering in the dark-adapted mouse. To obviate this problem, we divided and processed the OCT volume data in small subregions (Figs. 1C,D). The implementation of this approach

was achieved with fully automatic data postprocessing software.

Histology

For histology, normally light adapted mice were euthanized by carbon dioxide in the morning between 10 and 11 AM in the National Eye Institute (NEI) histology core facility. Enucleation and preparation of the tissue were performed immediately after euthanasia (3 mice, n = 6 eyes). Plastic embedding was performed with a protocol designed to rapidly preserve cellular relationships through freeze substitution, while enabling subsequent dissection and production of 1-µm-thick sections.[59] Briefly, enucleated eyes were first rapidly immersed in liquid propane at dry ice temperature for 1 minute. The eyes were then very rapidly transferred to a vial containing 20 mL of a mixture of 97% methanol and 3% acetic acid, prechilled to dry ice temperatures. The vial was then stored at -80° for 48 hours. After 48 hours, eyes were transferred to a -40° freezer for 4 hours. Because freeze-substituted tissue can be brittle and difficult to dissect, the acetic acid-methanol mixture was decanted and rapidly replaced with a mixture of 10 mL ethanol (EtOH) and 2 mL 25% EM-grade glutaraldehyde[59] prechilled to -40°. Eyes were stored for 48 hours at -40° in Glut-EtOH, then 24 hours at -20°, and finally 4 hours at room temperature. The Glut-EtOH was then replaced with 90% ethanol for 10 minutes. The anterior segment of the eye was next removed, and, while immersed in 90% EtOH, a region that encompassed ~1 mm of tissue centered on the optic nerve head was isolated for further processing. The tissue was then conventionally processed into Polybed 812 (Polysciences #08791-500, Warrington, PA) (i.e., equilibrated successively two times for 30 minutes in 100% ethanol and then in 100% propylene oxide). The tissue was further equilibrated in a 1:1 mix of propylene oxide:Polybed 812, and then 100% Polybed 812. Polymerization was achieved at 60° for 36 hours. Sections of 1.25 µm thickness were cut on a Leica EM UC7 ultramicrotome, stained with 1% toluidine blue, and mounted on microscope slides and secured under a coverslip with Permount mounting medium (Fisher Sci. #SP15-100). Sections were imaged with a confocal microscope (Nikon A1) using a 40× water immersion objective and operating in the transmitted light detector mode. To assess potential shrinkage artifacts, quantitative comparison was made of the distances between a number of histological features and the corresponding OCT hyperreflective bands (Fig. 3).

Results

Identification of a Novel ORG Backscatter Signal Potentially Arising from the ROS Tips

The ORG of the outer retina of the mouse exhibits multiple time-dependent scattering changes in response to a brief bleaching exposure. These changes are particularly prominent in hyperreflective bands corresponding to the retinal structures situated between and including the external limiting membrane (ELM) and BrM (Fig. 1E). In a previous study,[42] we assigned the strong scattering signal anterior and closest to that of BrM to the ROST. This signal was unusual in having an asymmetrical form that encompassed a time-varying extent of the ROS profile. The scattering profile of BrM, which is about 0.5 µm thick in mice[3] and much thinner physically than the axial OCT PSF, is thus expected to act effectively as a point scattering source for the A-scan. The scattering profile of BrM is well described by a Gaussian with a 3.6 µm FWHM (Fig. 2A, inset), providing confirmation of the theoretical description of the PSF. Similarly, we found that the hyperreflective band arising from the ELM, whose scattering source is also less than 1 µm thick, is well described by Gaussian with FWHM of 3.6 µm. These confirmations of the axial PSF underpin the application of a deconvolution algorithm with a Gaussian function having a FWHM of 3.6 µm to the OCT profile data.

OCT backscatter profiles obtained in the experiment of Figure 1 at five time points before and after the bleaching exposure ($t = 0$) are shown in Figure 2A, and the corresponding deconvolved profiles in Figure 2B. Deconvolution split the scattering peak located ~7 µm anterior to the BrM band into two distinct components, which we hypothesized to arise from the ROST and the RPE anterior surface, respectively, based on their positions (blue dashed box in Fig. 2B). We further analyzed the two components by fitting this portion of the deconvolved profile with the sum of two Gaussian functions. The summed Gaussians gave a good description of the data (Fig. 2C), so that the center position, width, and amplitude parameters of the fitted Gaussians were used to quantify the time-dependent changes in the profiles. Notably, the Gaussian decomposition revealed the newly resolved scattering peak more distant from that of BrM to have very nearly the same kinetics as the band corresponding to the RIS/ROS junctions (Fig. 2D), consistent with the ideas that it arises from the ROSTs, and that the mechanisms underlying the scattering changes at the two ends of the ROS are very similar. Although the scattering signal attributed to the apical RPE is substantially stronger than those from the RIS/ROS junction and the ROST, the similarity of its time course to those of the RIS/ROS and ROST suggests that a common kinetic process underlies all three signals (see Discussion).

The Backscatter Bands Resolved by Deconvolution have Positions Corresponding to the ROST and RPE Apical Surface as Defined by Histology

We performed confocal microscopy on albino mouse plastic sections to measure the distances between landmarks of the posterior retina (Fig. 3). In the magnified image (Fig. 3B) RPE cells with nuclei can be clearly seen, as well as the apical and basal surfaces of the RPE, the latter with submicrometer-thick BrM tightly apposed.[60] Here, we identify the "apical surface" of the RPE with the anterior edge of the darker staining region of the cells seen in the histology, while acknowledging that the apical microvillous processes are extensions of the surface. We hypothesize that the material density of the darker region of the cells is higher in the absence of melanin granules than in the microvilli, so that the darker region has a higher refractive index that constitutes a scattering boundary.

The average distance from BrM to the RPE apical surface was found to be 6.02 ± 0.07 µm from measurements at well-spaced locations from three eyes. The apical surface of the RPE exhibits numerous microvillous processes, many of which extend into the spaces between the ROST. These microvilli populate a gap of ~3.5 µm between the apical surface of the RPE and the ROSTs.

Investigative Ophthalmology & Visual Science

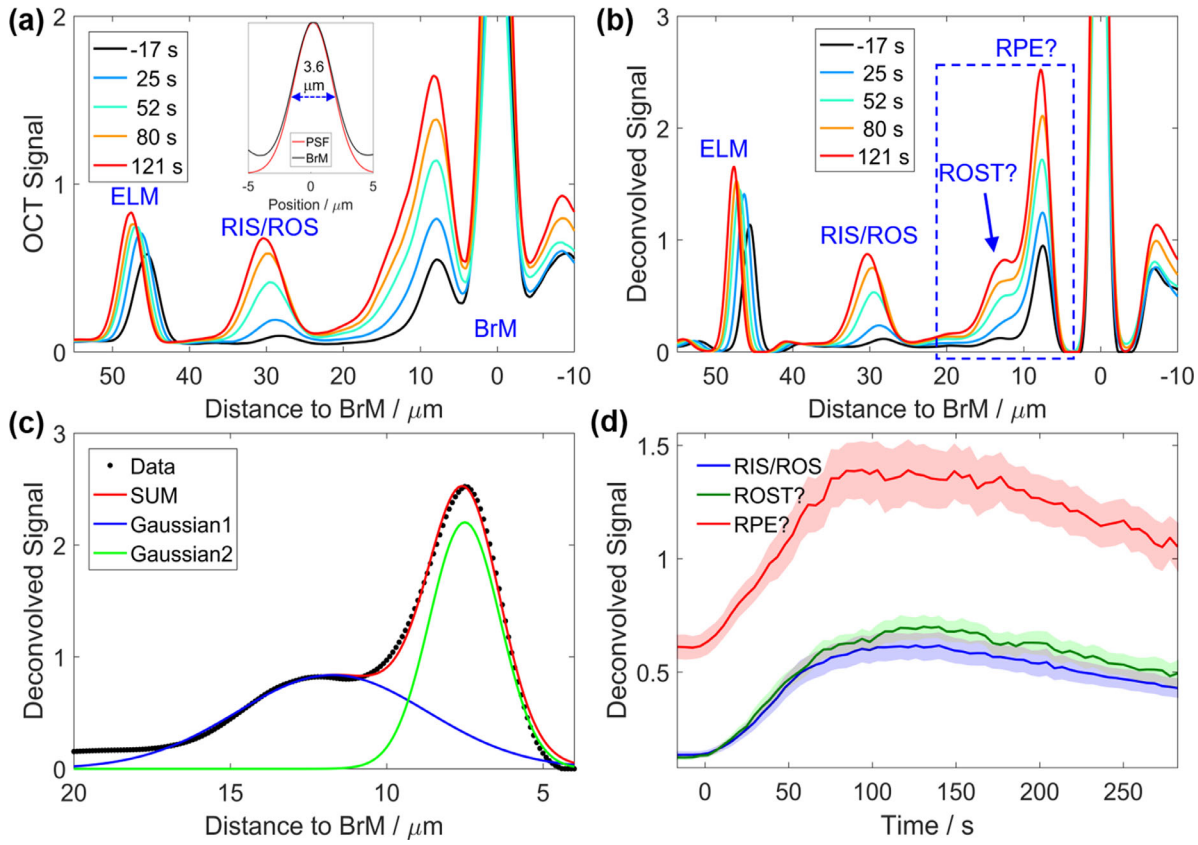

Figure 2. Deconvolution analysis reveals a novel distal scattering band whose optophysiological response matches that of the RIS/ROS. (**a**) Depth scattering profiles of the retina of an albino mouse allows clear visualization of backscatter bands from BrM, the RIS/ROS, and the ELM, but identification of the structures underlying the band immediately anterior to BrM is complicated by the changing shape of the band. (The inset compares the scattering band from BrM with a Gaussian of FWHM 3.6 μm.) (**b**) Deconvolution analysis reveals that the backscatter band nearest to BrM on the anterior side comprises two distinct components; the relative locations of the components suggest that the more anterior one might arise from the ROST and the more posterior one from the RPE apical surface (question marks are used to indicate that the assignment to structures required confirmation). (**c**) The components can be analyzed as the sum of two Gaussian functions, illustrated here by application to the highest amplitude signal in the blue-dashed box of (**b**), represented by the black dots. (**d**) Comparison of the kinetics and amplitude of the backscatter band from the RIS/ROS with the band tentatively ascribed to the ROST reveals them to have nearly identical amplitudes and kinetics; these signals are the averages from 11 eyes; the light-colored bands give the time-dependent SEM.

As an initial comparison of the OCT axial backscatter profiles and histology, we superimposed the average deconvolved OCT A-scan on the image of a retinal section from the same mouse (Fig. 3B, left). The OCT bands assigned to the ELM, RIS/ROS, and BrM line are seen to line up well with their presumptive histological correlates. In particular, the band (green Gaussian) closest to the BrM band is centered very nearly at the RPE apical surface in the image, while the center of the novel secondary band (blue Gaussian) coincides with the average position of the ROST. For statistical evaluation we measured distances from BrM in both histological sections and OCT axial profiles (Figs. 3C, D). When plotted against one another, the two sets of distance measurements are well described by a regression line with slope (1.076) near unity. Although the deviation from unity suggests an ~7% tissue shrinkage during fixation, the consistency of the fitted line as a description of all the data indicates there have been no differential shrinkage artifact. Moreover, the small variation in the positions of the OCT bands ascribed to the apical RPE and ROST show these OCT features to be highly stable across animals, with a separation corresponding closely to the average distance in the histology between the RPE apical surface and the ROSTs.

A further useful comparison can be made by considering the widths of the hyperreflective bands. Gaussians fitted to the nondeconvolved bands arising from the ELM and BrM have FWHM's corresponding closely to that of the OCT axial PSF, 3.6 μm (Fig. 2A, inset). This correspondence is expected because the ultrastructural elements in the retina responsible for the scattering in both cases have axial extents less than 1 μm, substantially smaller than the FWHM of the PSF, so that these structures act as "point sources" for the A-scans. In contrast, the Gaussians fitted to the deconvolved RIS/ROS and ROST bands have a FWHM of 6.2 μm and 7.2 μm, respectively. The histology clearly predicts that the bands arising from scattering by the RIS/ROS boundaries and the ROSTs would be wider than the bands arising from BrM and the ELM because the positions of the RIS/ROS of different rods are distributed over 3 to 5 μm, and the positions of the ROSTs are similarly distributed (Fig. 3G). In contrast, the narrow distribution of distances in the histology from BrM to the apical surface of the RPE (FWHM = 1.0 μm; Fig. 3F) predicts a correspondingly narrow width in the distribution of OCT distance. This prediction is borne out: the distance between the BrM band and the band attributed to the apical RPE (Fig. 2C) has a mean of 6.5 μm and sample standard

Investigative Ophthalmology & Visual Science

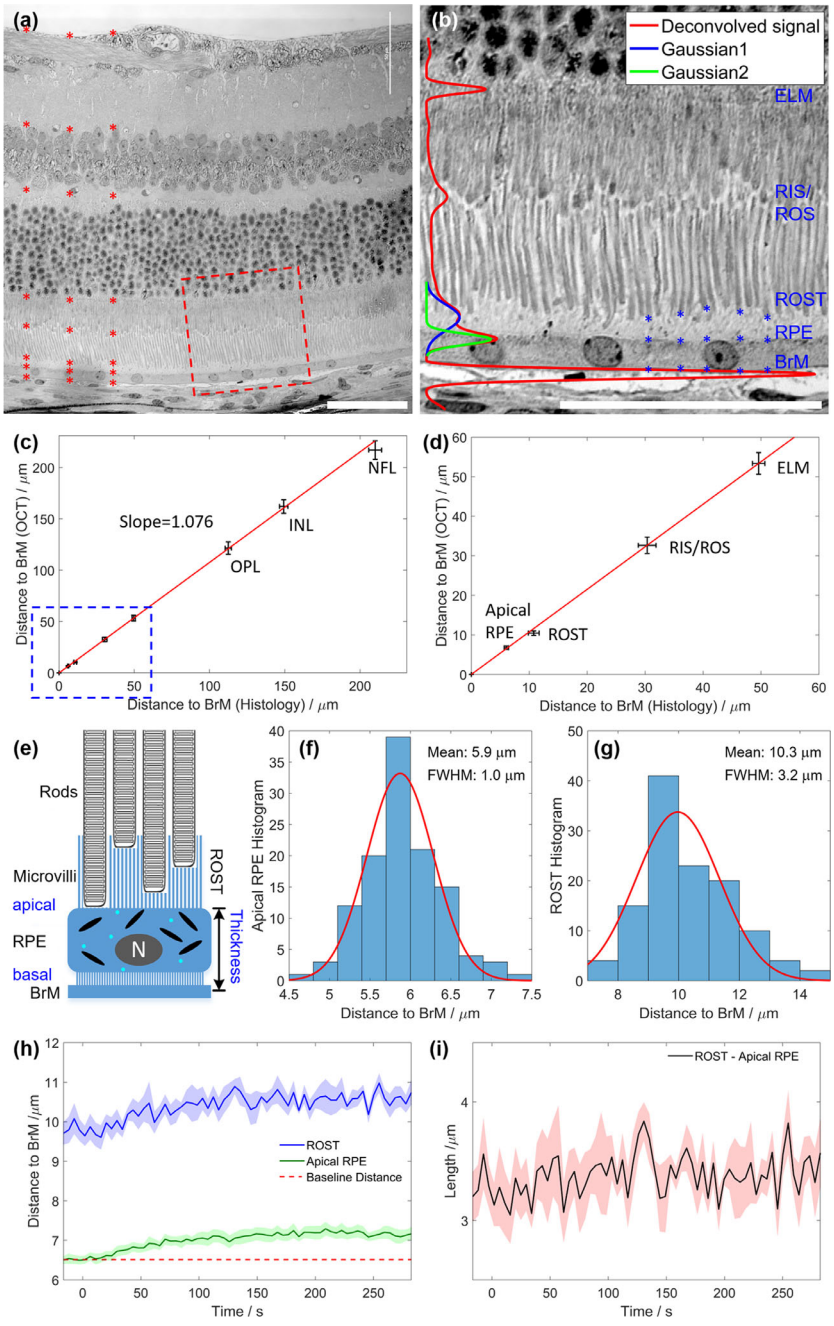

Figure 3. ROST and the RPE apical surface observed with histology correspond well with the assignment of the novel OCT bands resolved with deconvolution. (**a**) Confocal image of a plastic section of a B6-albino mouse retina; the superimposed red asterisks provide examples of measurements made along straight lines between BrM and the anterior surface of the retina for panels (**c**) and (**d**). (**b**) Magnified image of the region in panel (**a**) circumscribed by the red rectangle, with the deconvolved OCT line profile from the same eye superimposed; the blue asterisks provide examples of measurements made for panels (**f**) and (**g**). (**c**) Distances measured in histological sections (abscissa, as illustrated in panels (**a**), (**b**)) plotted versus distances measured with OCT to the hyperreflective bands corresponding to the histologically identified structure. The histology comprised 20 measurements, while the OCT data were averages from B-scans of 12 mice, error bars plot SDs. The reciprocal of the slope of the regression line (1/1.076 = 0.93) provides an estimate of tissue shrinkage during fixation. (**d**) Magnified view of the portion of panel (**c**) indicated by the blue rectangle, which comprises the portion of the retina between BrM and the ELM. (**e**) Schematic of the ROST to BrM complex; melanin granules (which are absent in the albino mice) are shown for generality. (**f**) Histogram of distances between BrM and the apical surface of the RPE (excluding the faint apical processes; see blue asterisks in (**b**) for example). (**g**) Histogram of distances between BrM and the ROSTs from 120 individual rods tips. The threefold greater FWHM of this histogram compared with that of panel (**f**) arises from the variation in the distal positions of the ROSTs. (**h**) Bleaching-induced displacements of the RPE and ROST OCT bands relative to that of BrM; (**i**) Difference between the traces in panel (**h**); the thickness of the subretinal space between the ROST and apical RPE remains nearly constant during the response. The results in (**h**) and (**i**) are the average of six experiments; the light-colored regions surrounding the traces represent ± 1 SEM. Scale bar in (**a**) and (**b**), 50 μm. The ordinate in panel (**i**) has been expanded from that in panel (**h**) to facilitate evaluation of stability. All histology and OCT measurements were measured from B6-albino mice.

Investigative Ophthalmology & Visual Science

deviation of 0.22 µm (n = 6 mice); a Gaussian probability distribution with a standard deviation of 0.22 has a FWHM of 0.6 µm, close to the value 1.0 µm obtained from the histology.

An alternative hypothesis that might explain the two OCT bands assigned to the ROST and RPE apical surface is that there are two distinct populations of rods with different ROS lengths. To test this hypothesis, we measured the axial position of the RIS/ROS and ROST of 120 rods whose ROS was completely visible in the histological images, and simultaneously measured the intersections of the projection of a line defined by the ROS with the RPE apical surface and with BrM (Fig. 3B). The histogram of the distances of ROSTs from BrM was monomodal (Fig. 3G), and so the results provide no support for the alternative hypothesis. Overall, then, the histological data confirm the assignment of the two distal scattering bands resolved by deconvolution as arising from the ROST and the RPE apical surface.

The effect of the activation of rod phototransduction on the positions of the OCT bands attributed to the ROST and RPE apical surface relative to that of BrM was measured in the standard ORG experiment[42] with a 10% bleaching exposure (n = 11; Fig. 3H). Both bands displaced slightly away from that of BrM, with very similar time courses and a common displacement amplitude of about 0.5 µm (Fig. 3H, I). These results, combined with the similar kinetics of the intensity variation of the bands attributed to the RIS/ROS, ROST, and apical RPE surface (Fig. 2D), raise the question whether these features can be accommodated by the osmotic hypothesis previously presented as an explanation of bleaching-induced ROS elongation and RIS/ROS scattering changes[42] (see Discussion).

Bleaching-Induced ROS Swelling is Invariant Over the Diurnal Cycle

The OCT axial profile bands corresponding to the RIS/ROS and the ROST potentially provide a means of investigating whether changes in the length of the ROS occur over the diurnal cycle. Ideally, in an experiment aimed at quantifying diurnal variation in ROS length, measurements would be made on individual fully dark-adapted mice at different times during an established circadian cycle. A difficulty in making such measurements, however, is that the intensities of the RIS/ROS and ROST bands are relatively weak in the dark-adapted state, so that measurement imprecision would make it difficult to detect a length change expected to be about 1/10th the ROS length, ~2 µm. During the rod optophysiological response to a bleaching stimulus, however, the RIS/ROS and ROST bands become much more prominent (Fig. 2), and so we designed the experiment to take advantage of this increased visibility. Briefly, in each experimental session on a given day, measurements were made first on a fully dark adapted mouse, and then after exposure to a 10% bleaching stimulus. Moreover, to minimize variation that could arise from the ocular curvature or spatial variation in the location of the OCT scan field, the experimental protocol was enhanced so that OCT volumes were periodically obtained of the entire bleached region, allowing confirmation from vascular maps that the same region of the retina was imaged in each session.

Results from an individual mouse in an experiment with ORG sessions at 6:30 am, 11 am and 3 pm are presented in Figure 4. The traces in panels A-C present deconvolved OCT profiles from the posterior retina acquired in the dark (black trace), and four times after the bleaching exposure. The insets give en face projections of the portion of the retina from which the OCT data were acquired in each session: the identical vascular pattern of these images establishes that the data were acquired from the same retinal region. The time courses of change in the distances from the BrM band to the other bands are plotted in Figures 4(D-G). The ELM results are very clear: the kinetics and magnitude of the bleaching-induced ELM displacement toward the vitreous is identical in the three sessions, with a peak displacement from the dark-adapted position of ~2 µm in each case (Fig. 4D). However, the traces obtained in the 6:30 AM session (red traces) are uniformly displaced farther toward the vitreous by about 1 µm relative to the traces obtained in sessions at 11 AM (cyan trace) and 3 PM (black).

The results for the RIS/ROS band are very similar to those for the ELM band, in that the trace for the RIS/ROS band acquired in the 6:30 AM session is clearly displaced upward by about 1 µm from those acquired in the 11 AM and 3 PM sessions, whereas overall the traces from the three sessions exhibit similar kinetics. Because the RIS/ROS band is very weak in the dark its position before stimulation, particularly in the 6:30 AM session, is less well determined than that of the ELM band. Nonetheless, the basically shared shape of the time courses of the displacements of the different bands strengthens the conclusion that the RIS are being displaced as rigid (noncompressible) bodies. Overall, we conclude that phototransduction initiated by the bleaching exposure triggers displacement of the RIS/ROS and the ELM toward the vitreous with approximately invariant kinetics and amplitude throughout the day. Strikingly, however, the positions of these scattering bands vary during the diurnal cycle, such that the bands are farther from BrM at 6:30 AM, both in the dark-adapted state (gray bar in Figs. 4D-G) prior and during the rod optophysiological response (purple bar).

The measurements of the RIS/ROS and ELM bands reveal that the RIS have an invariant length throughout the day, but are displaced toward the vitreous in the morning in the dark-adapted eye, and further displaced in the same direction by bleaching stimulation. To determine whether the displacements of the ELM and RIS/ROS bands are caused by corresponding changes in the ROS length, we measured the axial positions of the reflective bands assigned to the ROSTs and to the RPE apical surface over the day and in response to the bleaching stimulus (Figs. 4F,G). These latter two bands exhibit no positional variation in the dark-adapted state over the diurnal cycle, and with the possible exception of the 3:00 PM session, negligible positional change in response to bleaching. (In this latter case, we note the relatively high variation in the prestimulation baseline, and note further that if the 3 PM ROST band position does change in response to stimulation, it is about 0.5 µm closer to the RPE and BrM.) Taken together, these results suggest that the length of the ROS is greater around 6:30 AM than at later times in the day, and so we proceeded to repeat the experiment of Figure 4 on a population of mice. Assuming diurnally invariant kinetics of the RIS/ROS and ELM band position changes in response to light, and the lack of a material change in the positions of the ROST and apical RPE bands, we focused on distances measured at two times relative to delivery of the bleaching stimulus (1) in the dark adapted state before bleaching and (2) at the maximum of the optophysiological response, which occurs ~2 minutes after the delivery of the bleaching stimulus (Fig. 4E-G), purple bar).

Investigative Ophthalmology & Visual Science

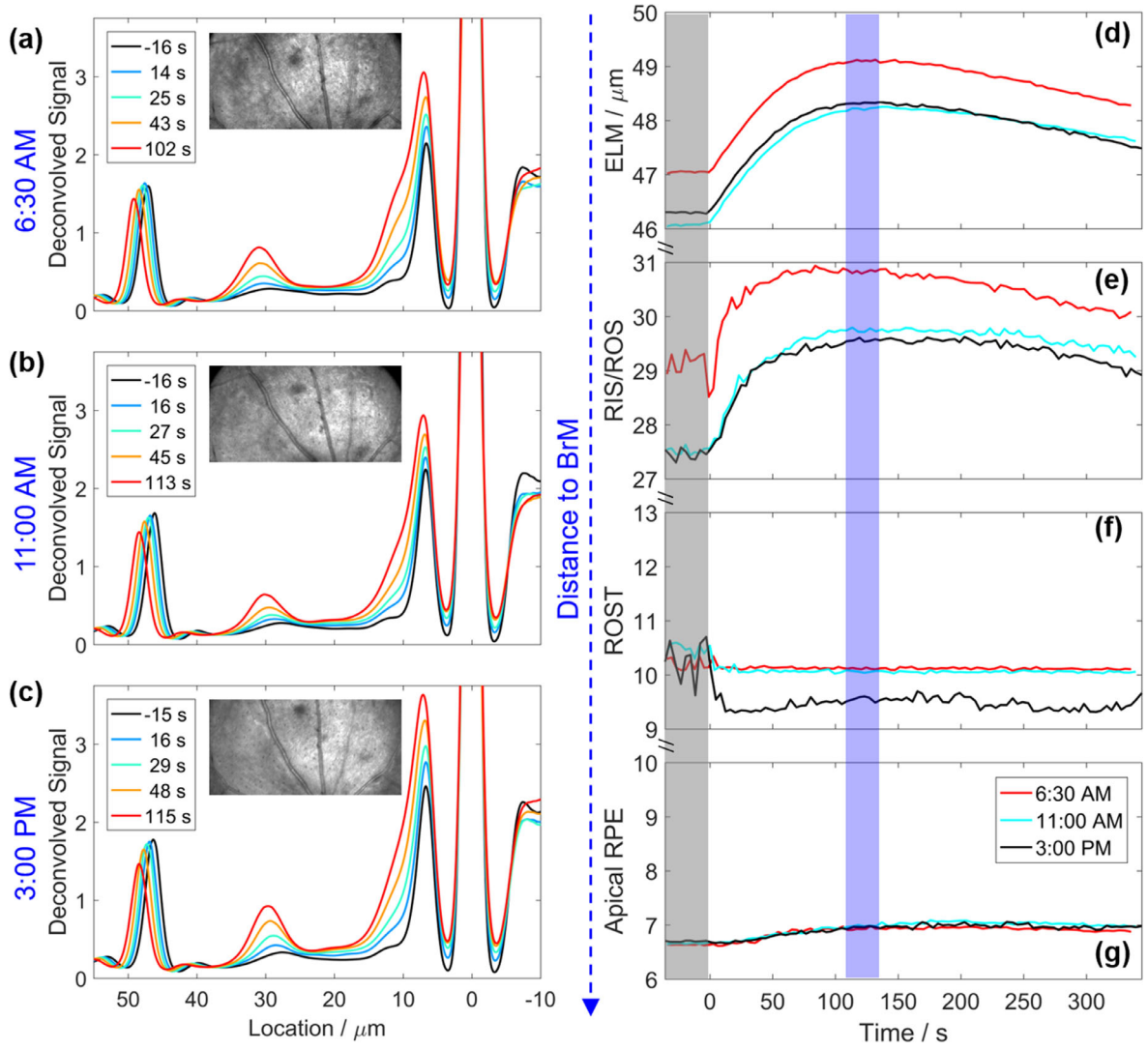

Figure 4. The experiment used to measure diurnal variation in ROS length in dark-adapted mice entrained to a 12:12 light:dark cycle with light onset normally at 7 AM. (**a–c**) Average OCT depth profiles measured at 6:30 AM, 11 AM and 3 PM before (black trace) and after various times (various colored traces) after exposure to a 488 nm light that bleached ~10% of the rhodopsin in the image field (inset, en face projections of OCT volume taken at the different times of the day in the day-long experiment). (**d–g**) Time course of the distances from the BrM band to the hyperreflective bands corresponding to ELM, RIS/ROS, ROST, and apical RPE, respectively. The mouse was kept dark adapted throughout the day, except for exposure to the 10% bleaching stimulus at 6:30 AM, 11 AM, and 3 PM. The mouse was anesthetized only for the relatively short time required for the ORG measurements, which took ~15 minutes in each case. Note that while the data in panels (**d**)–(**g**) are presented on an absolute scale that corresponds to retinal depth, there are gaps in the ordinates between the subpanels. The gray and purple bars represent the time at which measurements are extracted for statistical analysis of diurnal changes (Fig. 5). (The brief downward deflection in the red trace in (**e**) appears to be an artifact, as it is not present in all data sets.)

Diurnal ROS Length Variation is Revealed by Measurements of the Distance from ROS Tips to the RIS/ROS Boundary

Results from 11 experiments like that presented in Figure 4 are summarized in Figure 5, with measurements made in the dark-adapted state before the bleaching exposure presented on a gray background, and measurements made at the peak of the rod optophysiological response on white backgrounds. In this figure, symbols plot the measurements from individual experiments, with red color bars providing 95% confidence intervals, and blue color bars SD. Relative to their positions measured at 6:30 AM prior to normal light onset, the ELM and RIS/ROS bands showed highly reliable shifts, both in the dark, and at the peak of the bleaching response (Figs. 5A-C). In contrast, the ROST and apical RPE band positions were constant throughout the day, and likewise were the same whether measured in darkness or at the peak of the bleaching response (Figs. 5D-F). We derived the lengths of the RIS and ROS from the profile data of each mouse obtained at the peak of the bleaching response (Figs. 5G,H). While the RIS remained constant in length over the diurnal cycle, the ROS exhibited a highly reliable change in length, with the population means values of 17.7 ± 0.8, 15.9 ± 0.7, and 16.2 ± 0.8 μm (mean ± SEM) at 6:30 AM, 11 AM, and 3 PM, respectively. The maximal change in ROS length attributable to diurnal variation was 1.9 ± 0.4 μm, a 10.4% decrease by 11 AM from the length measured at 6:30 AM.

Investigative Ophthalmology & Visual Science

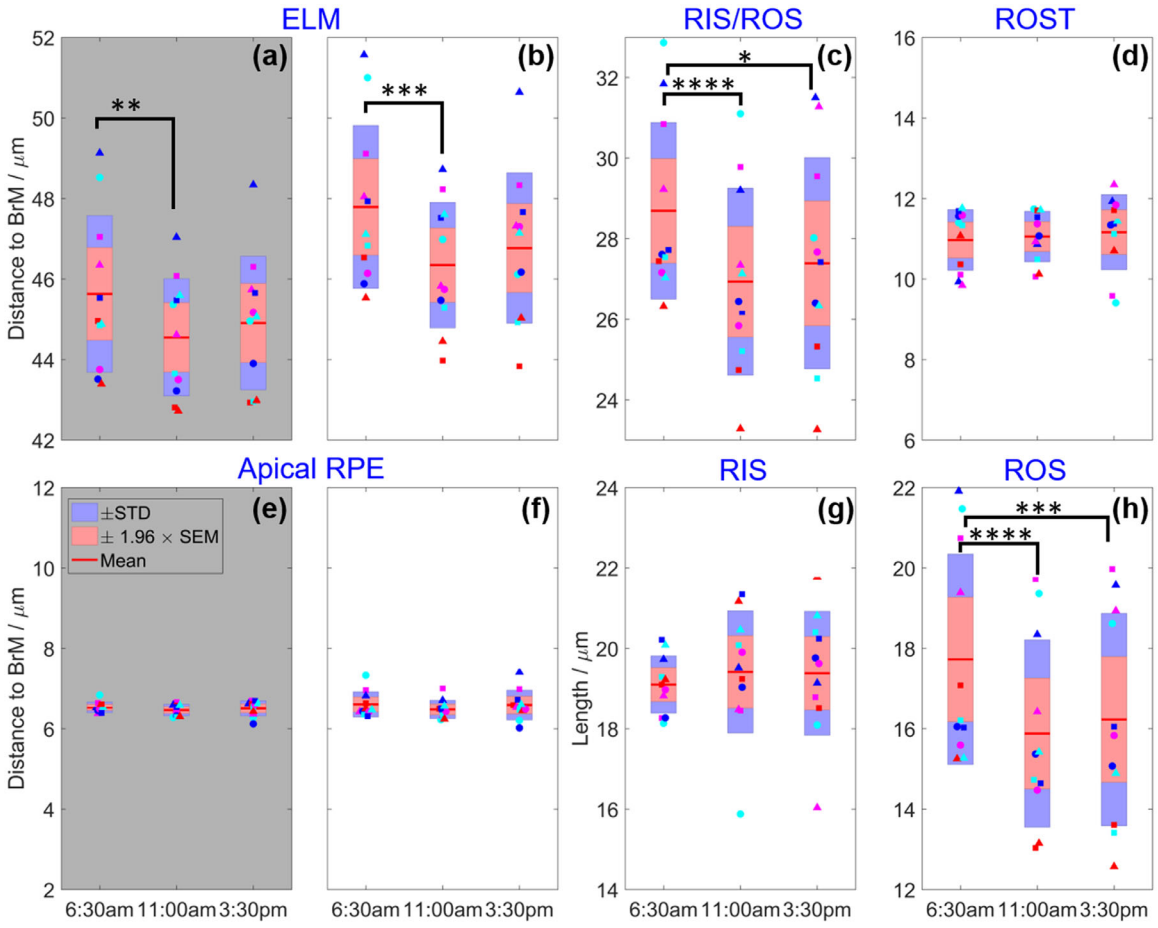

Figure 5. Summary of HR-OCT measurements made in individual mice in sessions at 6:30 AM, 11 AM, and 3:30 PM over one diurnal cycle. (**a–f**) Distances in the dark-adapted eye from the BrM band to other reflective bands (identified in large blue font above the panels); the measurements in (**a, b**) were extracted from data obtained in the dark adapted state, while those in (**c**)-(**f**) were taken ~125 seconds after a 10% bleaching exposure. (**g, h**) Lengths of the RIS and ROS measured as the distances between the RIS/ROS and ELM, and between the ROST and RIS/ROS bands. Each symbol presents the results of 1 of the 11 experiments. The average value of the measurements in each panel is presented as a red bar, while the light red error bar presents a 95% confidence interval and the light blue bar presents the sample SD. Statistical significance of paired *t*-tests versus results at 6:30 AM are indicated as follows: *$P < 0.05$, **$P < 0.01$, ***$P < 0.005$, ****$P < 0.0001$.

In previous experiments, we found that a 10% bleaching exposure produced a saturated amplitude fractional increase in ROS length of 0.11.[42] In the experiments reported here, the absolute increases in ROS length induced by the 10% bleaching exposure varied somewhat over the day, being 2.2 ± 0.09 µm, 1.76 ± 0.12 µm, and 1.86 ± 0.14 µm at 6:30 AM, 11 AM, and 3 PM, respectively. Remarkably, however, when divided by the average length of the dark-adapted ROS measured at the same three diurnal times prior to the exposure, the fractional increases in length induced by the bleach are 0.12, 0.11, and 0.12, respectively, virtually identical. This invariance in fractional elongation implies that the phototransduction-induced elongation scales with ROS length.

Mouse ROS Diurnal Length Variation Measured In Vivo is Consistent with Previous Ex Vivo Data

In designing the experiments presented in Figures 4 and 5, a number of factors had to be considered, including the time required to perform an individual set of measurements, the separation between measurements needed for adequate dark adaptation, and the practical limitations on the number of daily sessions for both mice and experimenters. Given that the mice were entrained to a vivarium 12 dark:12 light cycle with light onset at 7 AM, we selected the times for three daily sessions based on the experiments of Goldman et al.,[22] who quantified rod disc phagosomes in the RPE over the diurnal cycle. That study revealed that a large increase in RPE phagosomes occurred around an hour after the time of normal light onset. Thus, we designed our study in the hope of catching rods both before (6:30 AM), and not too long after (11 AM), a disc-shedding burst, as well as later in the day when some recovery of length might have occurred. A comparison between the results of that and two other studies[22,61,62] and those of this investigation are presented in Figure 6. To obtain a somewhat more complete picture of the diurnal cycle we made measurements on two additional cohorts of mice whose ROS length was measured at 2 hours and 23.5 hours respectively after the initial measurement at 6:30 AM, 30 minutes before normal light onset.

Investigative Ophthalmology & Visual Science

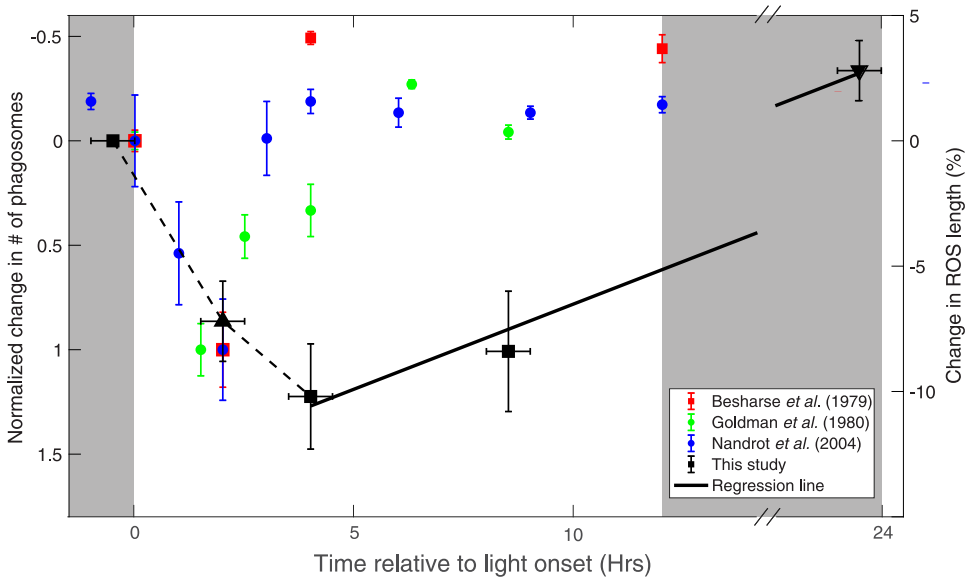

Figure 6. Comparison of diurnal changes in ROS length measured by OCT (black symbols and lines, right ordinate) with changes in phagosome count in the RPE of rats or mice from several studies[22,61,62] (colored symbols, left ordinate). The black-filled squares present data from the experiments of Figure 5 (n = 11), the black upward triangle results obtained at 9 AM (n = 12), and the black downward triangle (n = 9) results obtained ~23.5 hours, in each case after initial baseline measurements at 6:30 AM. The data points at 9 AM, 11 AM, and 3:30 PM are significantly less than zero ($P < 0.001$, $P < 0.0001$, $P < 0.001$, respectively). The point at 23.5 hours (+2.8%) is significantly greater than zero ($P = 0.03$). The solid black line presents a linear regression curve fitted to the OCT results obtained at 11 AM, 3:30 PM, and 24 hours, and has a slope of 0.68% hr^{-1} ($P < 0.0001$); for the average rod of length 17.7 µm, this corresponds to a ROS renewal rate of 2.9 µm/d. Normalized phagosome counts were obtained from the values reported by the studies by subtracting the pre-light-onset value and dividing by the maximum. Vertical error bars are ± SEM; horizontal error bars give the range of time for the experiments.

The diurnal changes in ROS length measured with OCT data compare favorably with the variation in RPE phagosome counts, in that highly reliable ROS shortening occurs around the time when the largest increase in phagosomes was measured. It bears emphasis, however, that although ROST shedding can be expected to coincide approximately with phagosome appearance in the RPE, growth by disc synthesis at the ROS base and phagosome digestion occur in different cells, and are governed by entirely distinct mechanisms. Thus, concurrence between the time courses of the two types of measurements is not expected, except near the time when a burst of shedding occurs. The ROS renewal rate estimated from the results at 11 AM, 3:30 PM, and 24 hours (0.68% $hour^{-1}$) corresponds to a disc synthesis rate of 0.12 µm/h for the average length ROS (17.7 µm) in the cohorts from which the measurements were obtained. If maintained through the diurnal cycle (including during the epoch of shedding), this rate of renewal would be 2.9 µm/d, somewhat higher than the average rate (2.2 to 2.5 µm/d) in a study that measured the synthesis rate in mice under a variety of lighting conditions.[63] However, the confidence interval for the slope of the regression line includes the value 2.5 µm/d, and moreover the observed 2.8% overshoot in ROS length at 24 hours contributed to the relatively high estimated renewal rate. This overshoot came from data of only one of the three cohorts, and could be a random effect.

Discussion

In this investigation we used OCT ORGs to measure the length of mouse ROS in vivo over the diurnal cycle in a well-defined region of the retina of individual albino mice. This effort was made possible by two advancements, the resolution by deconvolution of distinct OCT axial profile bands corresponding to the apical surface of the RPE and to the ROST (Figs. 2, 3), and the application of the phototransduction-driven rod optophysiological swelling response[42] (Figs. 2, 4), which strongly enhances the visibility of the RIS/ROS and ROST bands of the OCT backscattering profiles. In this context, it is notable that the ROS swelling response remained essentially invariant in amplitude and kinetics over the diurnal cycle in the dark-adapted eye, enhancing its value as a benchmark of function. In particular, ROS elongation in response to a 10% bleaching exposure remained constant throughout the diurnal cycle at 11% to 12% of the ROS length, despite highly reliable changes in average length over the day (Figs. 5, 6). The measurements are consistent with the conclusion that the observed diurnal variation in ROS layer thickness (Fig. 5H) arises from rod disc shedding and renewal. First, the largest measured change in ROS layer thickness occurs around the circadian time when the greatest amount of rod disc shedding has been shown to occur (Fig. 6).[22,61,62] Second, the estimated rate of ROS disc synthesis, 0.12 µm/h (Fig. 6), is within the range of renewal previously reported for mammalian rods.[9,15,61]

Bleaching-Induced Displacement and Scattering Changes of the OCT Bands Attributed to the ROST and Apical RPE

The similar kinetics of scattering intensity changes of the OCT axial profile bands attributed to the RIS/ROS, ROST,

and apical RPE (Fig. 2D), and likewise the parallel displacement of the OCTs bands ascribed to the ROST and RPE apical surface (Fig. 3H) call for a consistent explanation. This matter is addressable in the framework of the hypothesis that strong activation of rod phototransduction causes an increase in ROS osmolarity[42] and the auxiliary hypothesis that the water that enters the ROS in response to the osmotic stimulus originates in the choroid and sclera.[65] First, osmotically driven water movement into the ROS is rate-limited by very low water permeability of the ROS plasma membrane,[42] and so the time course of water movement at each location between the source and ROS sink should follow similar rate-limited kinetics. Second, because ROS disc membranes tend to fuse with the plasma membrane as they progress toward the ROS tip,[64] the increased surface area of the ROST should cause differential swelling in a manner parallel to that hypothesized to occur at the ROS base.[42] Thus, given that the ROS base and the ROST are at the opposite ends of a waveguide with the same refractive index between the two extremes, it can be expected from Fresnel theory that backscatter from the base and tips would have similar amplitude and kinetics (Fig 2D). Third, the hypothesis that the water underlying bleaching-induced ROS swelling originates in the choroid and sclera implies that during the ROS swelling response there is a time-varying gradient of water activity from the source to the ROS sink. This water would likely move through the RPE, which expresses functional aquaporin channels.[66] Water moving down such a gradient through the RPE will necessarily exert a pressure that could displace RPE apical processes and/or alter the distribution of refractive material in these processes (Fig. 3E), producing a change in backscattering by the RPE apical region (Fig. 2D), which would give rise to an apparent displacement of the scattering boundary (Fig. 3H). The amplitude of the scattering from the RPE apical surface cannot readily be computed with Fresnel theory in the manner applied to the RIS/ROS boundary[42] because the relevant refractive indices have not been determined. Although such ideas must be incorporated into a quantitative scheme to become a full-fledged explanation of these phenomena, they nonetheless show that the osmotic swelling hypothesis[42] in principle could be extended to account for all the bleaching-induced OCT band displacements and scattering changes from the RIS/ROS to BrM.

Comparison with Human Studies

Jonnal et al.,[11] using adaptive optics OCT, measured diurnal changes in the length of individual human cone outer segments (COS) in the near periphery (1.8° from the fovea) of three subjects. They found an average rate of COS growth of 2.4 µm/d, comparable to the rate of 2.9 µm/d estimated for the mouse rods of this study (Fig. 6). In a remarkable follow-up study, Kocaoglu et al.[12] observed abrupt decreases of 2.2 to 2.5 µm in the length of individual human COS, which are naturally interpreted as disc packet-shedding events. Several other studies have investigated diurnal variation in the outer retina of humans with OCT, but did not report COS length changes.[67–71] Pircher et al.,[67] however, observed bright reflection spots within the cone outer segments and the changing depth position of these spots corresponds to the expected COS growth rate. Read et al.[69] measured the retinal thickness of healthy adult subjects with SD-OCT every 2 hours from 9 AM to 7 PM, and found a small change in the thickness of the foveal outer retinal layers (IS/OS to RPE). The most likely reason that these latter studies did not observe changes in COS length is inadequate OCT axial (z-) resolution, compounded by spatial variation. Adaptive optics (AO) per se does not increase axial resolution, which is determined by the source coherence length of the OCT scanner; however, when AO is combined with an OCT source having adequate axial resolution, the capability of identifying individual cones in the x and y dimensions greatly facilitates the measurement of diurnal COS length variation.[11,12] In the experiments reported here, in addition to the short coherence length of the OCT, the relative homogeneity of the rod-dominant retina, and the ability to image the same locations in repeated sessions over the diurnal cycle were important factors contributing to the stability needed for measuring micrometer-scale changes.

ORG Experiments in Mice with Pigmented RPE

Due to the presence of melanin in the apical processes of their RPE cells, ROST cannot be resolved in OCTs of pigmented mice, and so only albino mice were used in this study. The retinas might be different between albino and pigmented strains in ways other than melanin, for example, rod density is less in some albino strains than in pigmented mice[72] and RPE65 polymorphisms give rise to differential light-damage susceptibility and rhodopsin regeneration rates.[54,73] Thus, it is possible that there are differences in disc shedding and renewal rates between pigmented and albino mice that would affect the comparison across strains and approaches (Fig. 6). Nevertheless, our previous study[42] shows that the ORG response is almost identical in albino and pigmented stains. Although a methodology for reliably determining the length of the ROS of pigmented mice in vivo has yet to be developed, investigation of albino mice has provided a foundation for the use of these mice in future studies of disc shedding and renewal, as it did in the past.[74]

Although the conclusions from the present investigation rests on results from populations of rods, it should be possible to extend the work to individual rods because investigations with AO-SLO has been able to resolve light reflected from individual mouse rods.[52,75,76] Ongoing efforts combining AO-OCT, AO-SLO system,[77,78] and/or speckle averaging OCT[79–81] in mouse photoreceptor imaging also show promise in distinguishing cone backscatter signals from those of the rods in the mouse photoreceptor mosaic. More generally, the approach used here, combined with AO-OCT and AO-SLO should afford efficient use of the ORG in mouse to screen for, and characterize molecular mechanisms that govern rod and cone disc shedding and renewal,[29,82,83] as well as the mechanisms underlying bleaching-induced outer segments swelling and scattering changes in the posterior eye.

Acknowledgments

The authors thank Sarah Karlen for assistance with mouse colony management. The authors thank Vivek Srinivasan for sharing software for OCT processing.

Supported by National Institutes of Health grants EY02660 (ENP), EY026556 (RJZ), EY012576 (NEI Core grant), and NSF I/UCRC CBSS Grant (RJZ).

Investigative Ophthalmology & Visual Science

Disclosure: **P. Zhang,** None; **B. Shibata,** None; **G. Peinado**, None; **R.J. Zawadzki,** None; **P. FitzGerald,** None; **E.N. Pugh Jr**, None

References

1. Carter-Dawson LD, Lavail MM. Rods and cones in the mouse retina. 1. Structural analysis using light and electron microscop. *J Comp Neurol.* 1979;188:245–262.
2. Curcio CA, Sloan KR, Kalina RE, Hendrickson AE. Human photoreceptor topography. *J Comp Neurol.* 1990;292:497–523.
3. Volland S, Esteve-Rudd J, Hoo J, Yee C, Williams DS. A comparison of some organizational characteristics of the mouse central retina and the human macula. *PLOS ONE.* 2015;10:e0125631.
4. Chinchore Y, Mitra A, Dolph PJ. Accumulation of rhodopsin in late endosomes triggers photoreceptor cell degeneration. *PLOS Genet.* 2009;5:e1000377.
5. Dryja TP, McGee TL, Reichel E, et al. A point mutation of the rhodopsin gene in one form of retinitis pigmentosa. *Nature.* 1990;343:364–366.
6. Rosenfeld PJ, Cowley GS, McGee TL, Sandberg MA, Berson EL, Dryja TP. A null mutation in the rhodopsin gene causes rod photoreceptor dysfunction and autosomal recessive retinitis pigmentosa. *Nat Genet.* 1992;1:209–213.
7. Arshavsky VY, Lamb TD, Pugh EN, Jr. G-proteins and phototransduction. *Annu Rev Physiol.* 2002;64:153–187.
8. Young RW. Shedding of discs from rod outer segments in the rhesus monkey. *J Ultrastruct Res.* 1971;34:190–203.
9. Young RW. The renewal of rod and cone outer segments in the rhesus monkey. *J Cell Biol.* 1971;49:303–318.
10. Young RW. The renewal of photoreceptor cell outer segments. *J Cell Biol.* 1967;33:61–72.
11. Jonnal RS, Besecker JR, Derby JC, et al. Imaging outer segment renewal in living human cone photoreceptors. *Optics Exp.* 2010;18:5257–5270.
12. Kocaoglu OP, Liu Z, Zhang F, Kurokawa K, Jonnal RS, Miller DT. Photoreceptor disc shedding in the living human eye. *Biomed Optics Exp.* 2016;7:4554–4568.
13. Zhang F, Liu Z, Kurokawa K, Miller DT. Tracking dynamics of photoreceptor disc shedding with adaptive optics-optical coherence tomography. *SPIE BiOS*: SPIE; 2017:8.
14. Xu J, Dodd RL, Makino CL, Simon MI, Baylor DA, Chen J. Prolonged photoresponses in transgenic mouse rods lacking arrestin. *Nature.* 1997;389:505–509.
15. LaVail MM. Kinetics of rod outer segment renewal in the developing mouse retina. *J Cell Biol.* 1973;58:650–661.
16. Reme´ C, Wirz-Justice A, Rhyner A, Hofmann S. Circadian rhythm in the light response of rat retinal disk-shedding and autophagy. *Brain Res.* 1986;369:356–360.
17. Besharse J, Dunis D. Methoxyindoles and photoreceptor metabolism: activation of rod shedding. *Science.* 1983;219:1341–1343.
18. Goldman AI. The sensitivity of rat rod outer segment disc shedding to light. *Invest Ophthalmol Vis Sci.* 1982;22:695–700.
19. Besharse JC, Dunis DA, Burnside B. Effects of cyclic adenosine 3′,5′-monophosphate on photoreceptor disc shedding and retinomotor movement. Inhibition of rod shedding and stimulation of cone elongation. *J Gen Physiol.* 1982;79:775–790.
20. Teirstein PS, Goldman AI, O'Brien PJ. Evidence for both local and central regulation of rat rod outer segment disc shedding. *Invest Ophthalmol Vis Sci.* 1980;19:1268–1273.
21. LaVail MM. Circadian nature of rod outer segment disc shedding in the rat. *Invest Ophthalmol Vis Sci.* 1980;19:407–411.
22. Goldman AI, Teirstein PS, O'Brien PJ. The role of ambient lighting in circadian disc shedding in the rod outer segment of the rat retina. *Invest Ophthalmol Vis Sci.* 1980;19:1257–1267.
23. LaVail M. Rod outer segment disk shedding in rat retina: relationship to cyclic lighting. *Science.* 1976;194:1071–1074.
24. Anderson DH, Fisher SK, Steinberg RH. Mammalian cones: disc shedding, phagocytosis, and renewal. *Invest Ophthalmol Vis Sci.* 1978;17:117–133.
25. Besharse JC, Pfenninger KH. Membrane assembly in retinal photoreceptors I. Freeze-fracture analysis of cytoplasmic vesicles in relationship to disc assembly. *J Cell Biol.* 1980;87:451–463.
26. Insinna C, Besharse JC. Intraflagellar transport and the sensory outer segment of vertebrate photoreceptors. *Dev Dyn.* 2008;237:1982–1992.
27. Ramamurthy V, Cayouette M. Development and disease of the photoreceptor cilium. *Clin Genet.* 2009;76:137–145.
28. Kevany BM, Palczewski K. Phagocytosis of retinal rod and cone photoreceptors. *Physiology (Bethesda).* 2010;25:8–15.
29. Mazzoni F, Safa H, Finnemann SC. Understanding photoreceptor outer segment phagocytosis: use and utility of RPE cells in culture. *Exp Eye Res.* 2014;126:51–60.
30. Goldberg AF, Moritz OL, Williams DS. Molecular basis for photoreceptor outer segment architecture. *Prog Retin Eye Res.* 2016;55:52–81.
31. Salinas RY, Pearring JN, Ding JD, Spencer WJ, Hao Y, Arshavsky VY. Photoreceptor discs form through peripherin-dependent suppression of ciliary ectosome release. *J Cell Biol.* 2017;216:1489–1499.
32. Spencer WJ, Ding JD, Lewis TR, et al. PRCD is essential for high-fidelity photoreceptor disc formation. *Proc Natl Acad Sci USA.* 2019;116:13087–13096.
33. Bizheva K, Pflug R, Hermann B, et al. Optophysiology: depth-resolved probing of retinal physiology with functional ultrahigh-resolution optical coherence tomography. *Proc Natl Acad Sci USA.* 2006;103:5066–5071.
34. Srinivasan VJ, Wojtkowski M, Fujimoto JG, Duker JS. In vivo measurement of retinal physiology with high-speed ultrahigh-resolution optical coherence tomography. *Optics Lett.* 2006;31:2308–2310.
35. Zhang QX, Lu RW, Wang BQ, Messinger JD, Curcio CA, Yao XC. Functional optical coherence tomography enables in vivo physiological assessment of retinal rod and cone photoreceptors. *Scient Rep.* 2015;5:1–10.
36. Li YC, Fariss RN, Qian JW, Cohen ED, Qian HH. Light-induced thickening of photoreceptor outer segment layer detected by ultra-high resolution OCT imaging. *Invest Ophthalmol Vis Sci.* 2016;57:OCT105–OCT111.
37. Insinna C, Besharse JC. Intraflagellar transport and the sensory outer segment of vertebrate photoreceptors. *Dev Dyn.* 2008;237:1982–1992.
38. Huang D, Swanson EA, Lin CP, et al. Optical coherence tomography. *Science.* 1991;254:1178–1181.
39. Wojtkowski M, Leitgeb R, Kowalczyk A, Bajraszewski T, Fercher AF. In vivo human retinal imaging by Fourier domain optical coherence tomography. *J Biomed Optics.* 2002;7:457–463.
40. Fercher AF, Drexler W, Hitzenberger CK, Lasser T. Optical coherence tomography - principles and applications. *Rep Progr Phys.* 2003;66:239–303.
41. Fischer MD, Huber G, Beck SC, et al. Noninvasive, in vivo assessment of mouse retinal structure using optical coherence tomography. *Plos One.* 2009;4:e7507.
42. Zhang P, Zawadzki RJ, Goswami M, et al. In vivo optophysiology reveals that G-protein activation triggers osmotic swelling and increased light scattering of rod photoreceptors. *Proc Natl Acad Sci USA.* 2017;114:E2937–E2946.

Investigative Ophthalmology & Visual Science

43. Lu CD, Lee B, Schottenhamml J, Maier A, Pugh EN, Jr, Fujimoto JG. Photoreceptor layer thickness changes during dark adaptation observed with ultrahigh-resolution optical coherence tomography. *Invest Ophthalmol Vis Sci.* 2017;58:4632–4643.
44. Zhang F, Kurokawa K, Lassoued A, Crowell JA, Miller DT. Cone photoreceptor classification in the living human eye from photostimulation-induced phase dynamics. *Proc Natl Acad Sci USA.s* 2019;116:7951–7956.
45. Hillmann D, Spahr H, Pfaffle C, Sudkamp H, Franke G, Huttmann G. In vivo optical imaging of physiological responses to photostimulation in human photoreceptors. *Proc Natl Acad Sci USA.* 2016;113:13138–13143.
46. Mulligan JB. The Optoretinogram at 38. *Optical Society of America Fall Vision Meeting: Symposium Honoring D I A MacLeod*. Reno, NV: NASA Technical Reports Server; 2018.
47. Harary HH, Brown JE, Pinto LH. Rapid light-induced changes in near infrared transmission of rods in Bufo marinus. *Science*. 1978;202:1083–1085.
48. Azimipour M, Valente D, Vienola KV, Werner JS, Zawadzki RJ, Jonnal RS. Optoretinography: optical measurements of human cone and rod photoreceptor responses to light. *bioRxiv*. 2019;10:4.
49. Azimipour M, Migacz JV, Zawadzki RJ, Werner JS, Jonnal RS. Functional retinal imaging using adaptive optics swept-source OCT at 1.6MHz. *Optica*. 2019;6:300–303.
50. Zhang PF, Zam A, Jian YF, et al. In vivo wide-field multispectral scanning laser ophthalmoscopy-optical coherence tomography mouse retinal imager: longitudinal imaging of ganglion cells, microglia, and Muller glia, and mapping of the mouse retinal and choroidal vasculature. *J Biomed Optics*. 2015;20:126005–10.
51. Zhang PF, Goswami M, Zawadzki RJ, Pugh EN, Jr. The photosensitivity of rhodopsin bleaching and light-induced increases of fundus reflectance in mice measured in vivo with scanning laser ophthalmoscopy. *Invest Ophthalmol Vis Sci.* 2016;57:3650–3664.
52. Zhang P, Mocci J, Wahl DJ, et al. Effect of a contact lens on mouse retinal in vivo imaging: effective focal length changes and monochromatic aberrations. *Exp Eye Res.* 2018;172:86–93.
53. Cesarovic N, Nicholls F, Rettich A, et al. Isoflurane and sevoflurane provide equally effective anaesthesia in laboratory mice. *Lab Animals*. 2010;44:329–336.
54. Lyubarsky AL, Savchenko AB, Morocco SB, Daniele LL, Redmond TM, Pugh EN, Jr. Mole quantity of RPE65 and its productivity in the generation of 11-cis-retinal from retinyl esters in the living mouse eye. *Biochemistry*. 2005;44:9880–9888.
55. Zhang P, Zam A, Jian Y, et al. Multispectral scanning laser ophthalmoscopy combined with optical coherence tomography for simultaneous in vivo mouse retinal imaging. *Proc. SPIE BiOS*. 2015;9307:93070H.
56. Leitgeb RA, Drexler W, Unterhuber A, et al. Ultrahigh resolution Fourier domain optical coherence tomography. *Optics Exp.* 2004;12:2156–2165.
57. Meleppat RK, Zhang P, Ju MJ, et al. Directional optical coherence tomography reveals melanin concentration-dependent scattering properties of retinal pigment epithelium. *J Biomed Optics*. 2019;24:1–10, 10.
58. Yun S, Tearney G, Bouma B, Park B, de Boer J. High-speed spectral-domain optical coherence tomography at 1.3 mum wavelength. *Optics Exp.* 2003;11:3598–3604.
59. Sun N, Shibata B, Hess JF, FitzGerald PG. An alternative means of retaining ocular structure and improving immunoreactivity for light microscopy studies. *Mol Vision*. 2015;21:428–442.
60. Bonilha VL, Rayborn ME, Bhattacharya SK, et al. The retinal pigment epithelium apical microvilli and retinal function. In: Hollyfield JG, Anderson RE, LaVail MM (eds), *Retinal Degenerative Diseases*. Boston, MA: Springer US; 2006:519–524.
61. Besharse JC, Hollyfield JG. Turnover of mouse photoreceptor outer segments in constant light and darkness. *Invest Ophthalmol Vis Sci.* 1979;18:1019–1024.
62. Nandrot EF, Kim Y, Brodie SE, Huang X, Sheppard D, Finnemann SC. Loss of synchronized retinal phagocytosis and age-related blindness in mice lacking alphavbeta5 integrin. *J Exp Med*. 2004;200:1539–1545.
63. Besharse JC, Hollyfield JG. Turnover of mouse photoreceptor outer segments in constant light and darkness. *Invest Ophthalmol Vis Sci*. 1979;18:1019–1024.
64. Chen C, Jiang Y, Koutalos Y. Dynamic behavior of rod photoreceptor disks. *Biophys J*. 2002;83:1403–1412.
65. Zawadzki RJ, et al. Light induced water movement in the outer retina investigated by Optical Coherence Tomography. *IOVS*. 2019;60(9), ARVO Abstract 1294.
66. Stamer WD, Bok D, Hu J, Jaffe GJ, McKay BS. Aquaporin-1 channels in human retinal pigment epithelium: role in transepithelial water movement. *Invest Ophthalmol Vis Sci*. 2003;44:2803–2808.
67. Pircher M, Kroisamer JS, Felberer F, Sattmann H, Götzinger E, Hitzenberger CK. Temporal changes of human cone photoreceptors observed in vivo with SLO/OCT. *Biomed Optics Exp.* 2011;2:100–112.
68. Jo Y-J, Heo D-W, Shin Y-I, Kim J-Y. Diurnal variation of retina thickness measured with time domain and spectral domain optical coherence tomography in healthy subjects. *Invest Ophthalmol Vis Sci.* 2011;52:6497–6500.
69. Read SA, Collins MJ, Alonso-Caneiro D. Diurnal variation of retinal thickness with spectral domain OCT. *Optom Vision Sci.* 2012;89:611–619.
70. Han YS, Lim HB, Lee SH, Kim JY. Diurnal variation in choroidal and retinal thickness of the early treatment of diabetic retinopathy study macular subfields determined using swept-source optical coherence tomography. *Ophthalmologica*. 2015;233:192–197.
71. Burfield HJ, Carkeet A, Ostrin LA. Ocular and systemic diurnal rhythms in emmetropic and myopic adults. *Invest Ophthalmol Vis Sci.* 2019;60:2237–2247.
72. Grant S, Patel NN, Philp AR, et al. Rod photopigment deficits in albinos are specific to mammals and arise during retinal development. *Visual Neurosci.* 2001;18:245–251.
73. Wenzel A, Reme CE, Williams TP, Hafezi F, Grimm C. The Rpe65 Leu450Met variation increases retinal resistance against light-induced degeneration by slowing rhodopsin regeneration. *J Neurosci*. 2001;21:53–58.
74. Jeffery G. The albino retina: an abnormality that provides insight into normal retinal development. *Trends Neurosci*. 1997;20:165–169.
75. Geng Y, Dubra A, Yin L, et al. Adaptive optics retinal imaging in the living mouse eye. *Biomed Opt Exp.* 2012;3:715–734.
76. Wahl DJ, Zhang P, Mocci J, et al. Adaptive optics in the mouse eye: wavefront sensing based vs. image-guided aberration correction. *Biomed Opt Exp*. 2019;10:4757–4774.
77. Zhang P, Miller EB, Manna SK, Meleppat RK, Pugh EN, Jr, Zawadzki RJ. Towards in vivo imaging of the mouse cone photoreceptors. *Proc. SPIE BiOS*. 2019;10858:08.
78. Zhang P, Wahl DJ, Mocci J, et al. Adaptive optics with combined optical coherence tomography and scanning laser ophthalmoscopy for in vivo mouse retina imaging. *Proc. SPIE BIOS*. 2018;10474:27.
79. Zhang P, Miller EB, Manna SK, Meleppat RK, Pugh EN, Jr, Zawadzki R. Temporal speckle-averaging of optical coher-

Investigative Ophthalmology & Visual Science

ence tomography volumes for cellular resolution neuronal and vascular retinal imaging. *Neurophotonics*. 2019;6:1–13, 13.

80. Miller EB, Zhang P, Ching K, Pugh EN, Jr, Burns ME. In vivo imaging reveals transient microglia recruitment and functional recovery of photoreceptor signaling after injury. *Proc Natl Acad Sci USA*. 2019;116:16603–16612.
81. Zhang P, Manna SK, Miller EB, et al. Aperture phase modulation with adaptive optics: a novel approach for speckle reduction and structure extraction in optical coherence tomography. *Biomed Opt Exp*. 2019;10:552–570.
82. Campbell LJ, West MC, Jensen AM. A high content, small molecule screen identifies candidate molecular pathways that regulate rod photoreceptor outer segment renewal. *Sci Rep*. 2018;8:14017.
83. Kevany BM, Palczewski K. Phagocytosis of retinal rod and cone photoreceptors. *Physiology (Bethesda, Md)*. 2010;25:8–15.

Investigative Ophthalmology & Visual Science